JOURNAL OF SOLID STATE CHEMISTRY 50, 51–69 (1983)

High Resolution Electron Microscopic Study of Tin Dioxide Crystals

DAVID J. SMITH, L. A. BURSILL,* AND G. J. WOOD

*High Resolution Electron Microscope, University of Cambridge, Free School Lane, Cambridge CB2 3RQ, England and *School of Physics, University of Melbourne, Parkville, Victoria 3052, Australia*

Received December 9, 1982; in revised form July 5, 1983

Crystals of Sb-doped tin dioxide have been examined by high resolution electron microscopy (≤2.3 Å point-to-point resolution) in [100], [001], and [1$\bar{1}$1] zone axes projections, and images of twin interfaces, inclined defects, and a possible crystallographic shear plane have been recorded. Image simulations confirmed that the metal atom rows have been clearly resolved in each of these three low-index projections for specific electron-optical conditions. Image observation and consideration of the possible atomic arrangements about a (011)-type twin interface suggested that this resulted from a glide operation given by $\frac{1}{2}\langle 1\bar{1}1\rangle$ (011) and a very close match with an experimental through-focal series was obtained using computer image simulations. The structural determination of crystal defects by high resolution electron microscopy is briefly discussed.

1. Introduction

Tin dioxide, which has the cassiterite—or rutile-type—crystal structure, is of interest as a catalyst when doped with antimony, and is also being investigated for its electrical characteristics as a semi-conductor. Pyke *et al.* (*1*) have examined crystals grown pure, and doped with a few percent Sb, in both reduced and fully oxidized states, using X-ray diffraction and optical and electron microscopy. No evidence was found for crystallographic shear structures, in marked contrast to the behavior of the corresponding reduced rutiles derived from TiO_2, although some Sb-doped crystals were observed to be twinned about (011). Furthermore, two alternative models for the twin composition plane were proposed, both of which seemed plausible on crystal chemistry grounds as well as being consistent with electron diffraction patterns and relatively low magnification diffraction contrast images.

This paper reports a high resolution (ca. 2 Å) electron microscopic examination of similar crystals of tin dioxide in three low index zones, namely [100], [001], and [1$\bar{1}$1]. Our aim was to search for defects in Sb-doped SnO_2 in each of these zones in order to locate Sb-rich regions, either in the form of extended defects (e.g., crystallographic shear planes), precipitates, or new "small" (cluster-type) defects which may have been missed by earlier lower resolution studies. Images showing a variety of defects including twin interfaces, inclined faults, and a possible crystallographic shear plane were obtained (Sect. 3). Image simulations (Sect. 4) confirmed the impression that the positions of the metal atom rows may be located in each of the three projections and that, under well-defined experimental conditions, it may be possible to interpret some

0022-4596/83 $3.00

experimental defect images at this level of resolution. The atomic arrangement at a (011)-type twin interface was then studied in detail (Sect. 5) using comparisons of computer simulations with experimental images: that good agreement was obtained without requiring the presence of any antimony was of particular interest given the widespread occurrence of twin boundaries in antimony-doped tin oxide catalysts (*1*, *2*).

2. Experimental

Crystals of Sb-doped SnO_2 (approximately 1 at.%) were supplied by Dr. M. D. Shannon (ICI Corporate Laboratories, Runcorn, U.K.); these were originally grown by Tilley (for details, see (*1*)). Crystals were black in color (blue in thin section), and prepared for electron microscopy by crushing under methanol in an agate mortar with pestle, and allowing a drop of dispersion to dry onto a lacey carbon film. Thin crystal edges lying over holes in this support film were carefully tilted into the {100}, {001}, and {1$\bar{1}$1} zone axes.

The observations reported here were obtained with a 600-kV instrument (*3*, *4*) with the electron-optical parameters

$$V_A = 500 \text{ kV}; \qquad C_s = 3.5 \text{ mm}; \qquad C_c = 3.5 \text{ mm}$$

where C_s and C_c are, respectively, the spherical and chromatic aberration coefficients of the objective lens. Images were typically recorded at magnifications of about 330,000× using 4½-sec exposures and defocused illumination. Correction of image astigmatism was normally carried out at 750,000× or more using the granularity of the carbon support.

Image simulations, using the multislice formulation based on the Cowley–Moodie *n*-beam dynamical diffraction theory [*5*], were carried out on both a Cyber 7600 computer and an IBM 370/165. Images were generated with a high density of data points and 256 gray levels; then the output was transferred via magnetic tape onto a photographic negative using an Optronics P1500 Photo-Write instrument.

3. Observations

(*a*) [*001*] *Projection*

When crystals were *flat* and symmetrically oriented into the [001] zone, the images were dominated by 3.3 × 3.3-Å spacings, in agreement with computer simulations for aligned crystals and axial illumination. However, images recorded in this zone characteristically show the rapid local variation in contrast, together with the appearance of 4.7 × 4.7-Å periodicities in thicker crystals, which have been discussed previously in terms of the breakdown in the screw symmetry operations of the space group of SnO_2 associated with crystal bending (*6*, *7*). In deformed crystals, there is an effective loss of the screw symmetry operations which accentuates crystal tilt effects. Figures 1a–d, for example, are a through-focal series of images (at about 380-Å intervals) of an elastically deformed crystal viewed in the [001] direction. Note the remarkable variation in image detail, both within a given micrograph and between corresponding areas of successive micrographs—elastic strains associated with dislocations very strongly affect the symmetry and intensity of the image detail. The 3.3 × 3.3-Å array intuitively expected for this projection of SnO_2 is only seen along the edge of the crystal. There was no indication of any "small" defects which could be associated with Sb-rich regions.

(*b*) [*1$\bar{1}$1*] *Projection*

Several members of a through-focal series of images for a crystal oriented in this

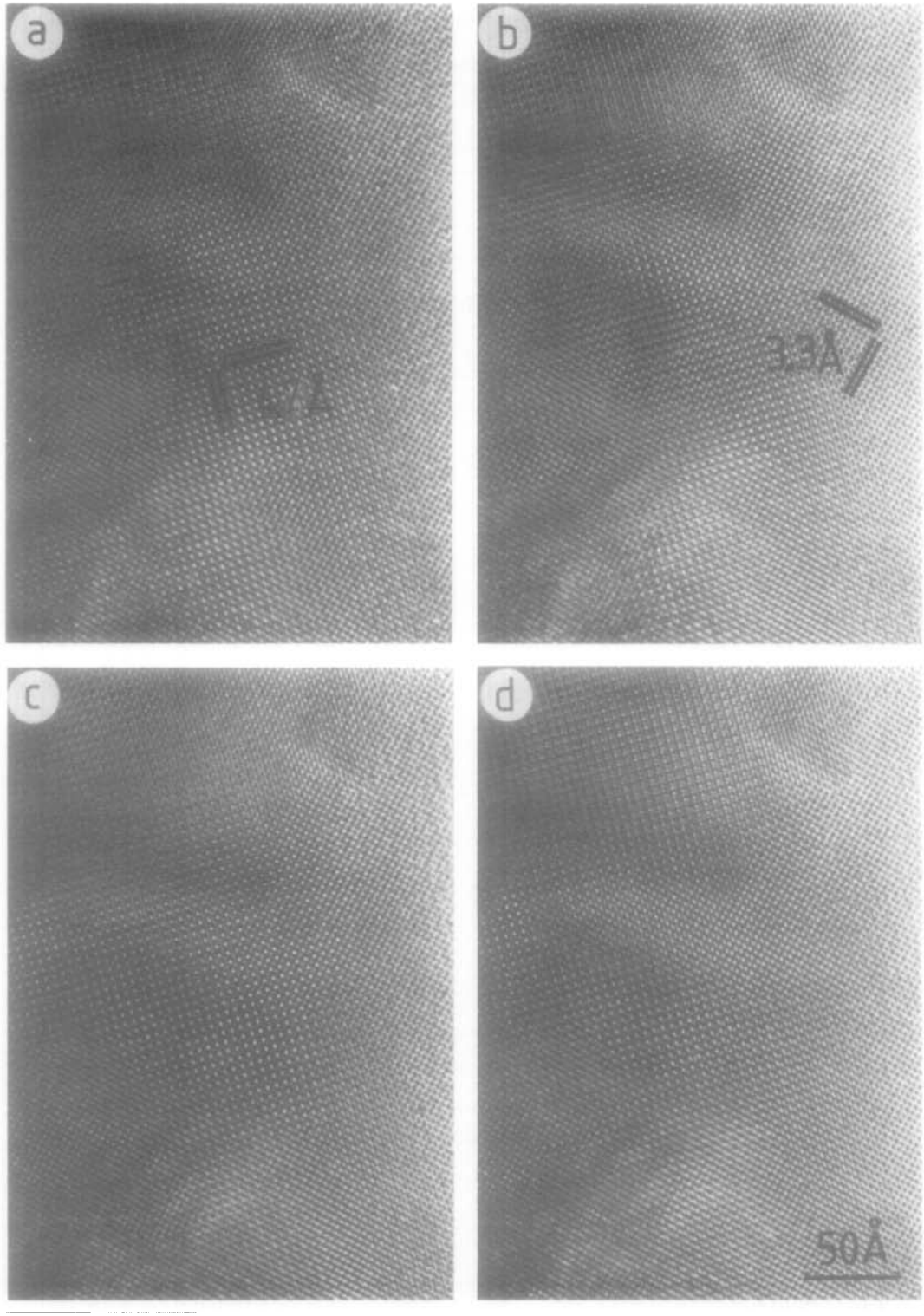

FIG. 1. Through-focal series (focal steps ~+380 Å) of SnO_2 crystal in the [001] projection at 500 kV. Note that 3.3-Å square arrays are only clearly seen along the crystal edge.

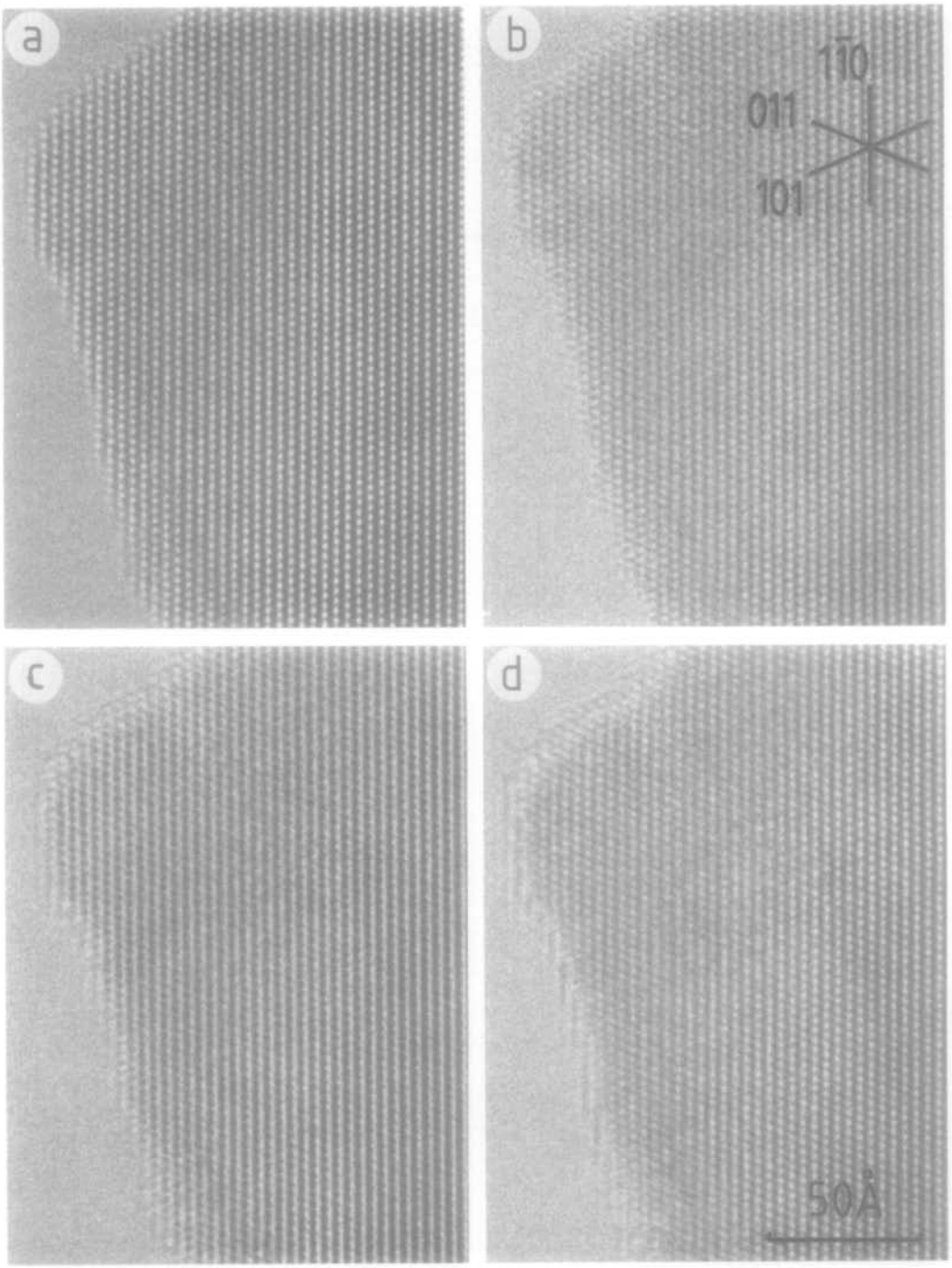

FIG. 2. Through-focal series (focal steps ~ -380 Å) of SnO_2 crystal in the $[11\bar{1}]$ projection at 500 kV.

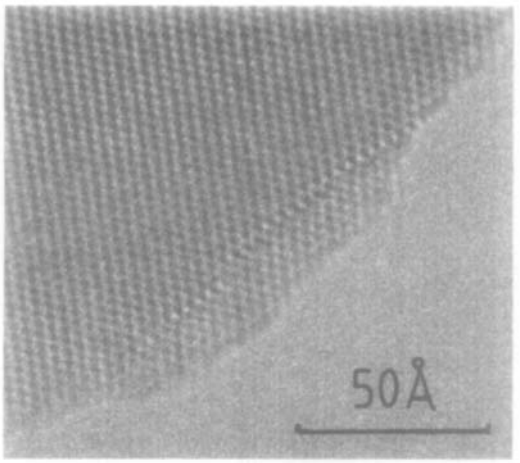

FIG. 3. Solitary image of a small planar defect resembling a *CS* plane having a $\frac{1}{2}\langle 0\bar{1}1\rangle$ (132) *CS* operation.

projection are shown in Figs. 2a–d. Note the absence of any contamination or amorphous surface layer; hence the corresponding image of the crystal edge is seen with unusual clarity, especially in Fig. 2a where the Fresnel fringe is minimal. Also note the reversals of image contrast from Fig. 2b to c and back again for d, as well as the fine structure in the Fresnel fringes of Figs. 2c and d.

Figure 3 shows a solitary example of an image of a planar defect which appears to have the characteristics of a crystallographic shear (*CS*) plane. The orientation is parallel to (132), and the lattice rows are displaced by $\frac{1}{2}d_{\bar{1}10}$, $0d_{011}$ and $\frac{1}{2}d_{10\bar{1}}$, consistent with a $\frac{1}{2}\langle 0\bar{1}1\rangle$ (132) *CS* operation. No evidence for other novel defects was found in this zone.

(*c*) [*100*] *Projection*

Images of SnO_2 recorded in this projection are shown in Figs. 4 to 8. The first of these, shown at low magnification, has an (011) lamella to the left of the field of view together with a complex array of defects to the right. These appear to be aligned along (011), with the image contrast suggesting twinning of the $(01\bar{1})$ fringes. The image contrast is dominated by arrays of white and black spots having the topology of the [100] projection of the metal atom arrangements of SnO_2. The contrast was found to be extremely sensitive to specimen orientation with asymmetries, and even changes from white to black spots on crossing the interface, appearing as the crystal is tilted off the zone. A small region showing approximately square symmetry (label A) can also be seen making an angle of about 7–10° with $(01\bar{1})$. The defects on the right are shown at higher magnification in the through-focal series given in Figs. 5a–d; observation along $(01\bar{1})$ clearly indicates the presence of several micro-twin lamellae.

Figure 6 shows an area where the image contrast is especially interesting—the white spots have split into two, giving images closely resembling the much discussed images of silicon and other tetrahedrally bonded semi-conductors (*8, 9*). These so-called "atom pair" images represent an artifact of the imaging conditions and, as will be shown later, appear at various defoci and over a range of crystal thicknesses.

Figures 7a–d show a through-focal series of images (about 380-Å intervals) in an area containing both an extended defect and a small micro-twin (arrowed) at the very edge of the crystal. While there are gradual changes in white (black) spot contrast moving in from the crystal edge, in the region of the defect the changes are quite complex and strongly focus-dependent. For example, in Fig. 7a, the (011), (020) and $(01\bar{1})$ lattice fringes show a smooth bending or displacement across the defect, whereas in Fig. 7c, (020) is practically continuous while $(01\bar{1})$ and (011) show marked discontinuity with a small region (~15 Å) where the fringes appear to suffer shifts of about one-half of a lattice spacing. A similar, though slightly more complex, description can be applied to Fig. 7b. Note the small

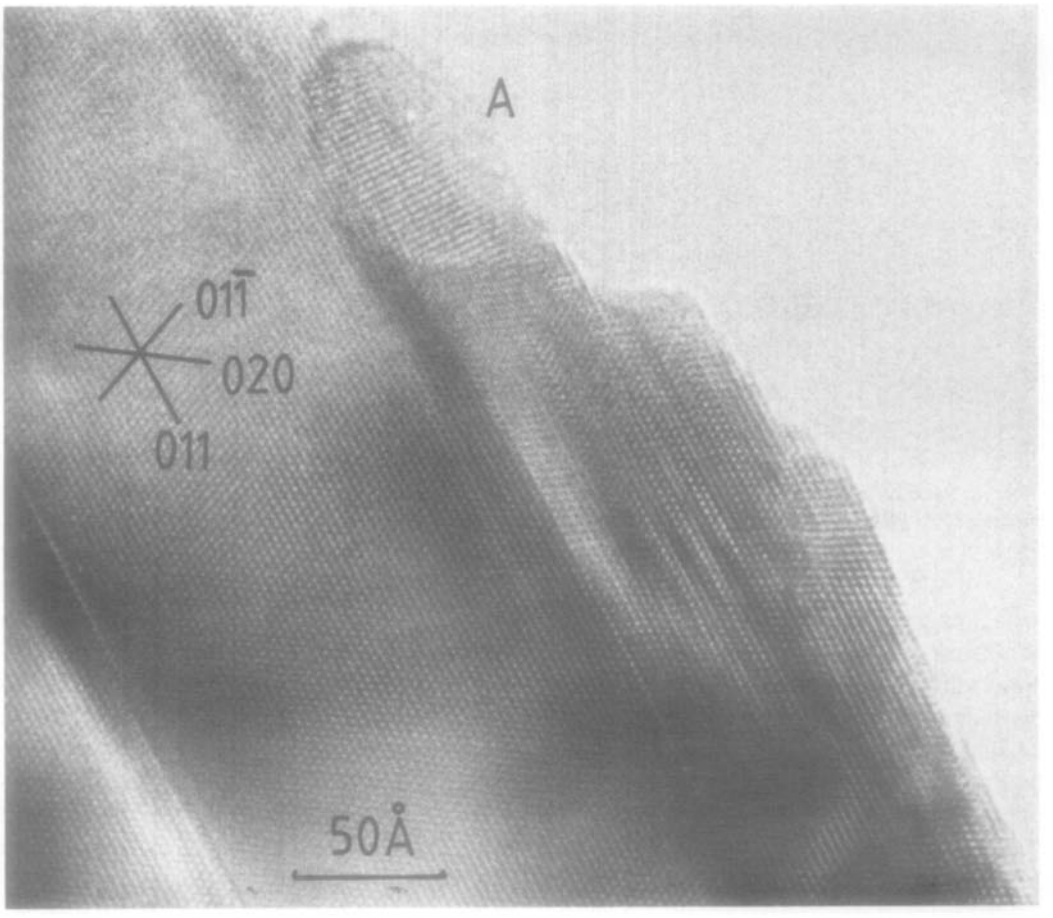

FIG. 4. Region of SnO_2 crystal viewed in the [100] projection showing an apparent (011) lamella to the left, a region of micro-twin lamellae to the right, and a small region having approximately square symmetry (labeled A).

patches superimposed on the SnO_2 lattice image, particularly in c and d, which resemble the contrast expected for amorphous material.

A through-focal series of images of a micro-twin lamella viewed along [100] is shown in Figs. 8a–f. The lamella varies in width from approximately $9 \times d_{011} = 23$ Å at the bottom, ending with an apparent partial dislocation at the top. Note that the twin interfaces appear in projection as a simple mirror operation, either centered on a row of white dots (Figs. 8b, c, and d), or black (Figs. 8a, e) depending upon defocus. The contrast reversal at the twin boundary closely resembles the contrast reversal within the SnO_2 matrix. Although the fine detail again changes in a complex manner with defocus, an additional terminating fringe at the top end of the micro-twin can be observed in all members of the through-focal series by sighting along the (011) planes. Wider twin lamellae (up to 50 Å thick) were observed in some areas.

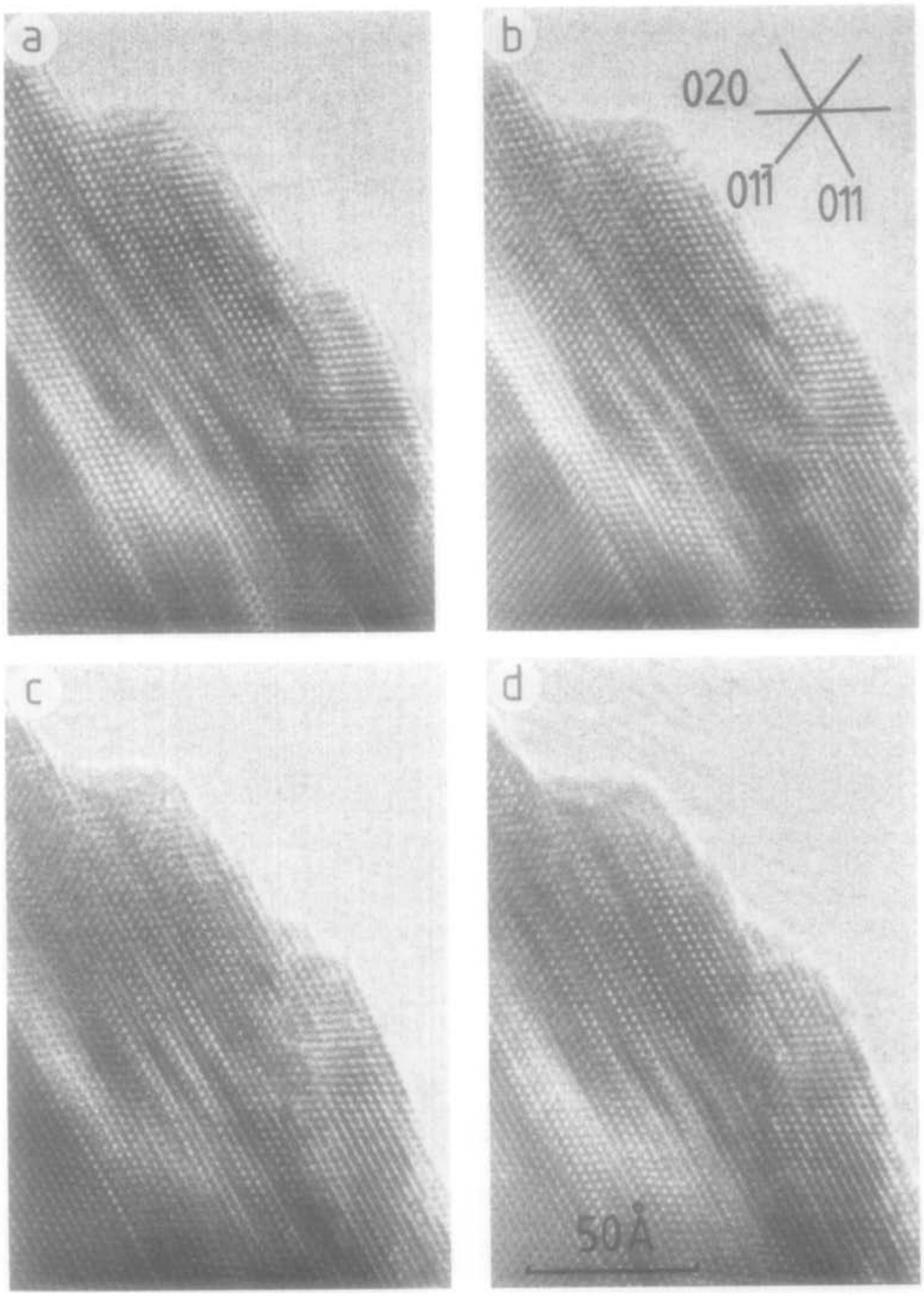

FIG. 5. Through-focal series (focal steps ~−380 Å) of region shown in Fig. 4. Note the rapid change in appearance of the (011) micro-twin lamellae.

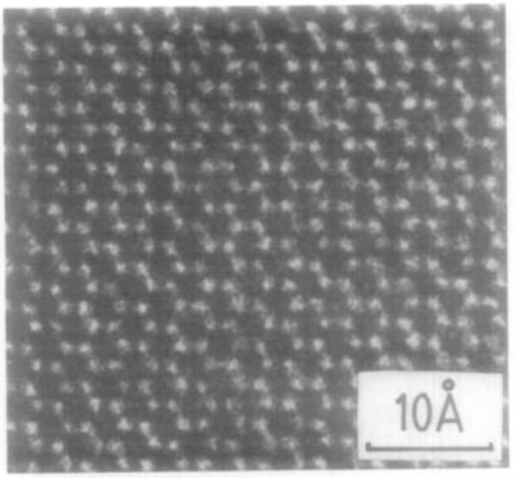

FIG. 6. Thicker region of SnO_2 crystal in [100] projection. "White spot" contrast seen at edge of crystal splits into a horizontal pair of white spots with separation of ~1.5 Å.

4. Image Simulations of Perfect SnO_2 Crystals

The crystal structure of SnO_2 is tetragonal, space group $P4_2/mnm$, with lattice parameters $a = 4.7373$ Å and $c = 3.1864$ Å and position parameter $u = 0.307$ (10). Figure 9 shows models of the structure projected in the major low index zones, namely [100], [1$\bar{1}$1], and [001], and Table I lists some of the larger interplanar spacings. Shortest distances between neighboring cation columns in these three projections are 2.85, 2.88, and 3.35 Å, respectively.

As well as being dependent on crystal structure, high resolution electron micrographs are sensitive functions of crystal thickness and alignment, objective lens defocus and microscope resolution, and the "fixed" microscope parameters of accelerating voltage (i.e., electron wavelength) and objective lens aberration coefficients, C_s (spherical) and C_c (chromatic). From Fig. 9 it is clear that, in order to determine the cationic positions in the three major projections, at least 2.37-Å resolution is required. Initially, images were simulated using considerably better resolution, namely 1.7 Å, thereby including the next major periodicity after 2.37 Å in each of the three projections considered. These computations also included a sharp aperture cutoff, since to include properly the effects of beam divergence (spatial coherence) and focal spread (temporal coherence) is rather more time-consuming. However, later simulations for detailed image matching and analysis purposes used a full treatment.

Figure 10 provides through-focal series of simulated images in the three zones using the parameters of the high voltage microscope, namely, $V_A = 500$ kV and $C_s = 3.5$ mm. The extreme sensitivity of the images to defocus changes is readily apparent in all three projections. It is also interesting to note that images resembling "atom pairs" are obtained in [100], at certain defoci, even for crystals as thin as 28 Å. Figure 11 illustrates the image behavior for increasing thickness in each of the zones at the optimum defocus of −865 Å. Comparison with the corresponding structural models in Fig. 9 shows that the cationic positions are generally reproduced as black spots in images of thin ($H \leq 120$ Å) perfect crystals (except only in [111] for $H \leq 25$ Å). Note the differences in "extinction" effects of the various diffracting beams with increasing thickness: in [001], "half-spacing" detail is produced, whereas in [100] and [11$\bar{1}$] the image

TABLE I

LOW INDEX INTERPLANAR SPACINGS IN TIN DIOXIDE

[100] zone		[1$\bar{1}$1] zone	
"010"	4.74 Å		
"001"	3.19 Å	011	2.64 Å
011	2.64 Å	121	1.76 Å
020	2.37 Å	220	1.67 Å
002	1.59 Å		
022	1.32 Å		

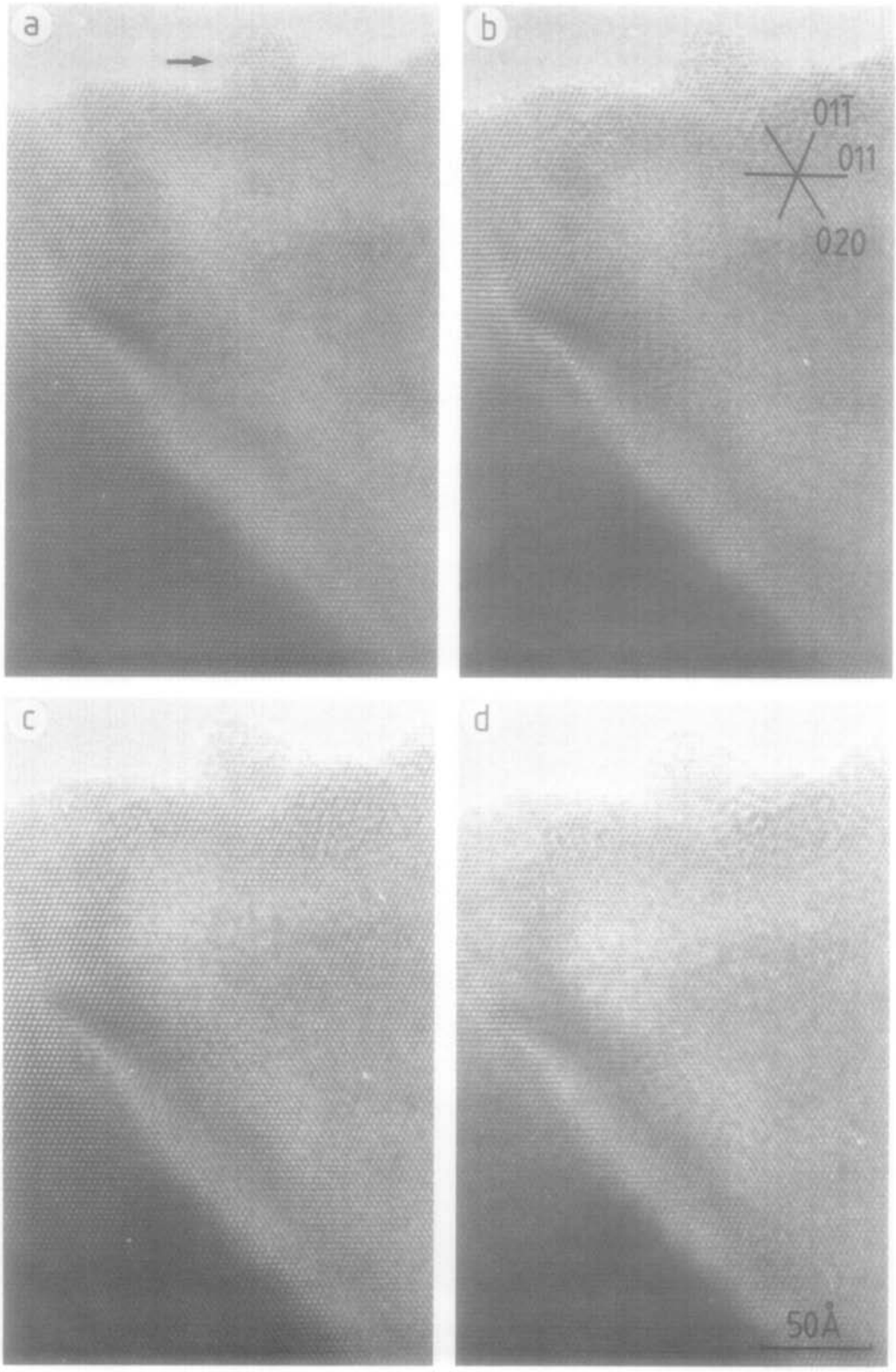

FIG. 7. Through-focal series (focal steps ~ −380 Å) of SnO_2 crystal in the [100] projection at 500 kV. Note the small micro-twin (arrowed in a) at the edge of the crystal and the complex lattice fringe behavior across the extended defect.

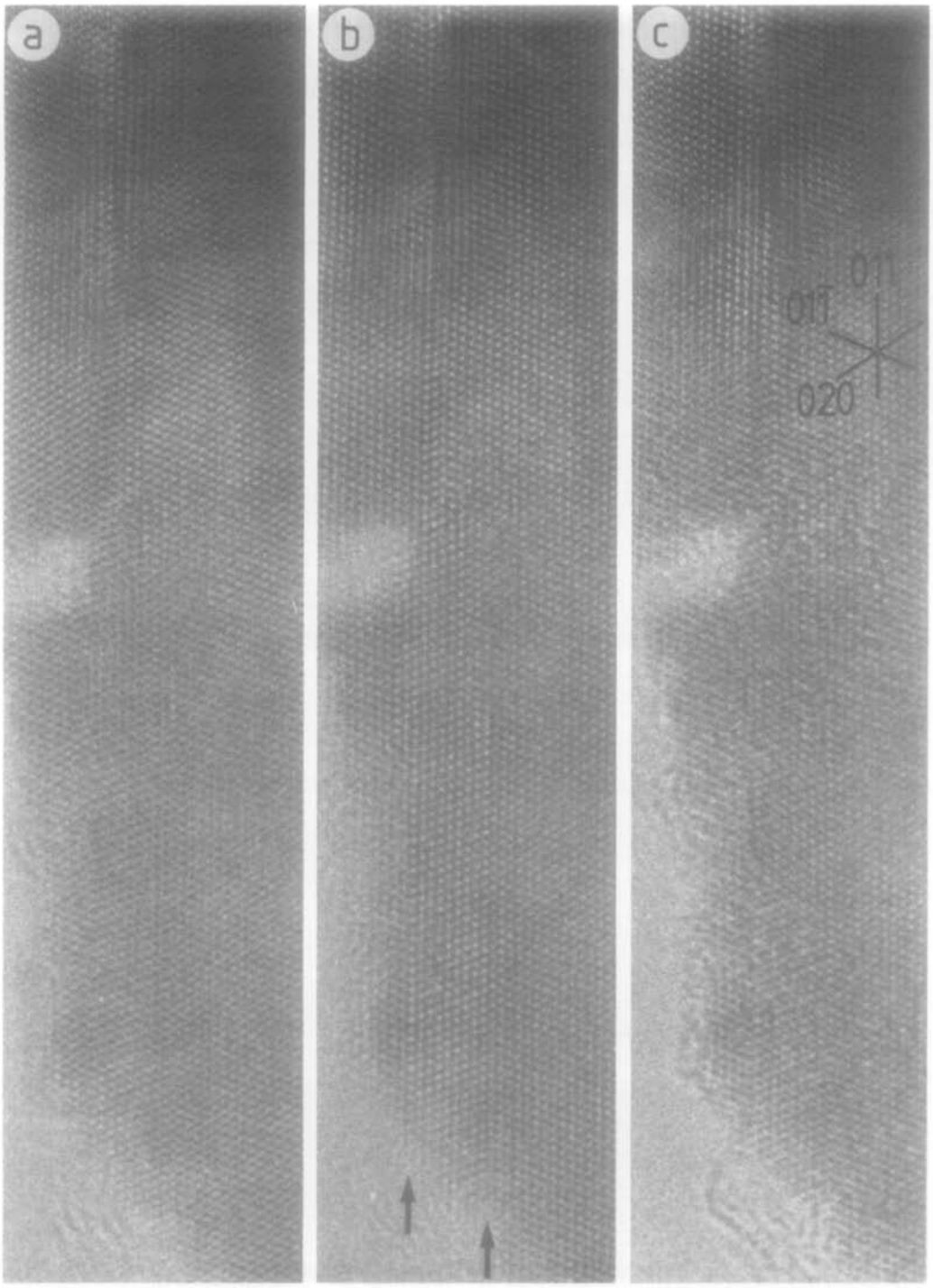

FIG. 8. Through-focal series (focal steps ~−380 Å) of (011) micro-twin lamella, decreasing in width from ~23 Å (arrowed) and terminating with an apparent partial dislocation (at top).

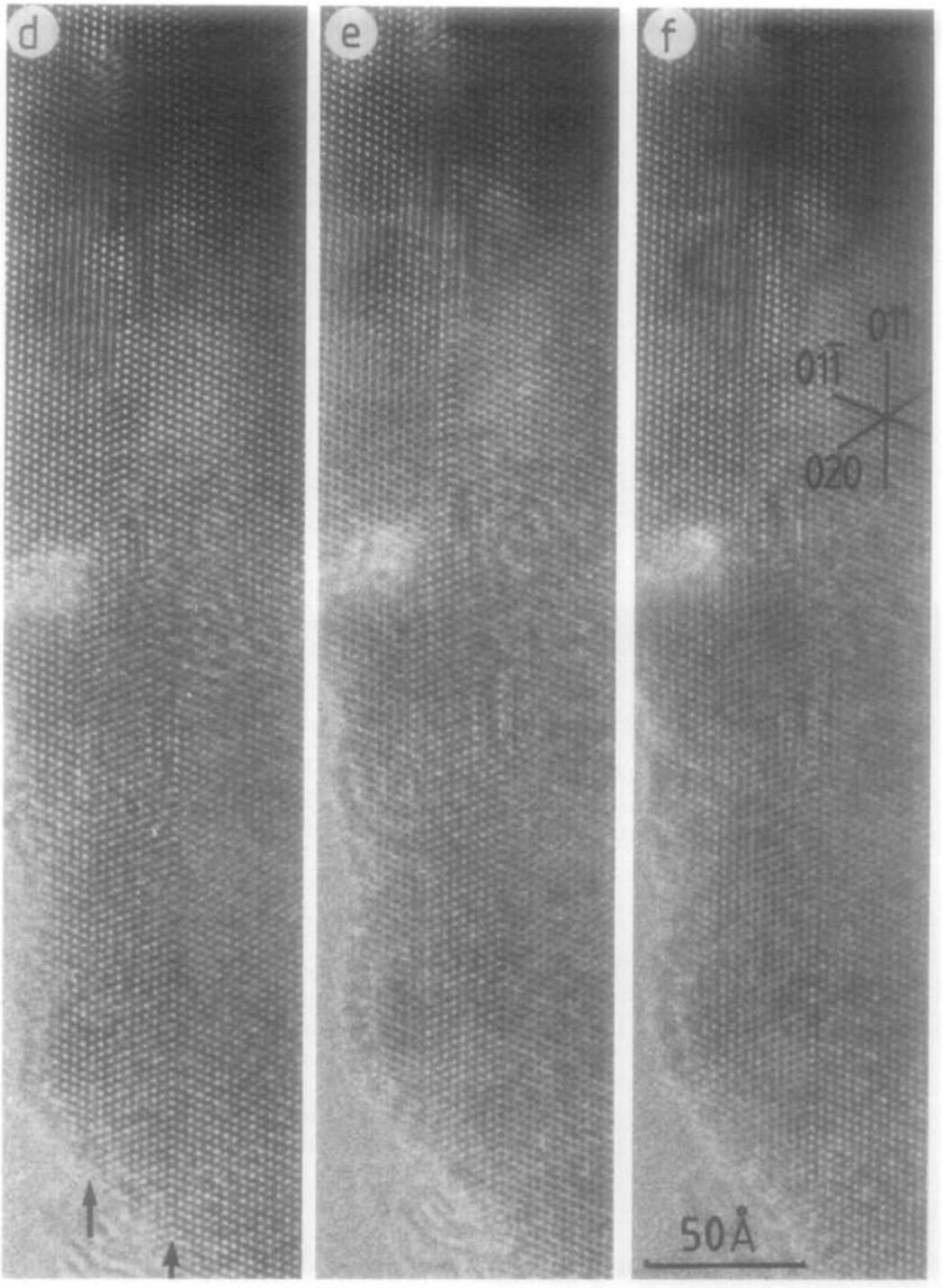

FIG. 8—*Continued.*

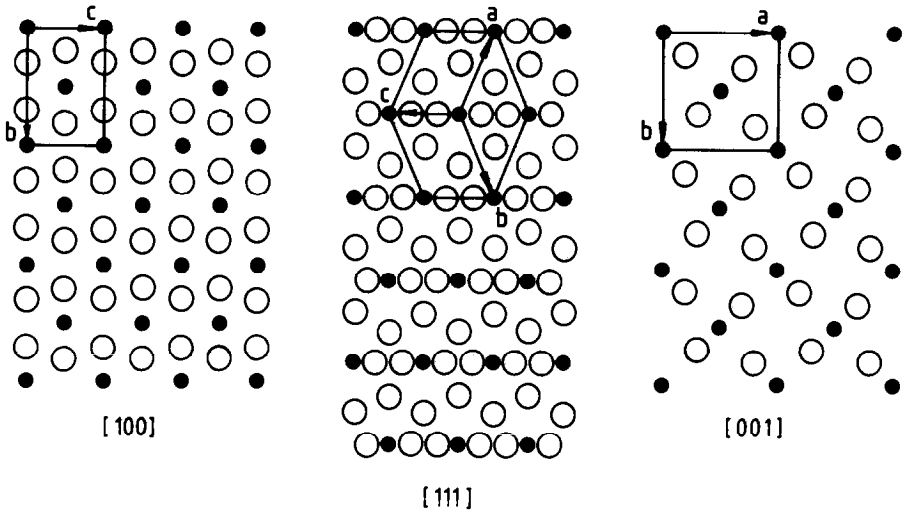

FIG. 9. Structure models of SnO_2 in the [100], [111], and [001] projections, with unit cell dimensions outlined, Sn cations (●); O anions (○).

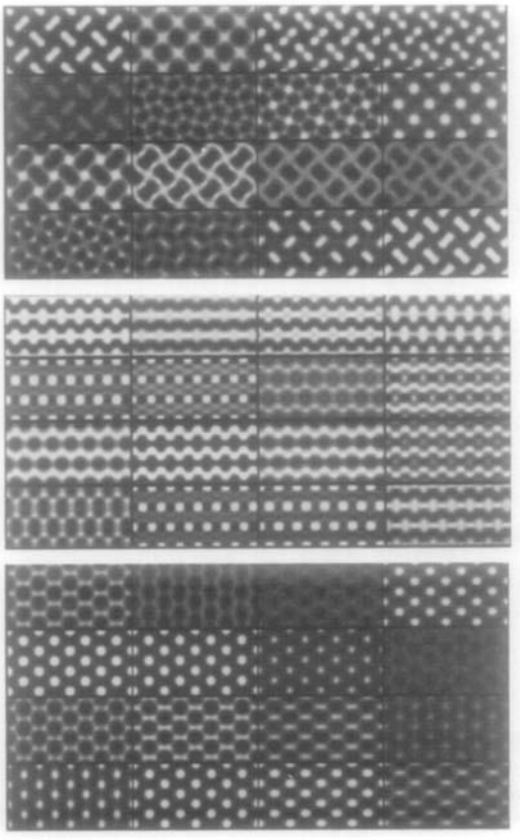

detail becomes predominantly one-dimensional.

A major problem with image matching of experimental micrographs is a lack of knowledge of the objective lens defocus value and the local crystal thickness. In the former case, it is helpful to study the characteristics of the Fresnel fringe occurring at the edge of a crystal—if necessary, it is possible to use simulations and image matching to work back to the defocus (*11*). Alternatively, if there is any amorphous material at the edge of the crystal, then optical diffraction analysis techniques might possibly be used, although this is often not sufficiently sensitive around Scherzer defocus (*12*) which is the major region of interest for high resolution electron microscopy. A further complication is that the optimum defo-

FIG. 10. Through-focal series of simulated images for SnO_2 at 500 kV with C_s = 3.5 mm. Top [001], 31.9 Å thick; middle [1$\bar{1}$1], 29.7 Å thick; bottom [100], 28.4 Å thick. Each series starts at −1400 Å (top left), with +100 Å steps (from left to right), finishing at +100 Å (bottom right).

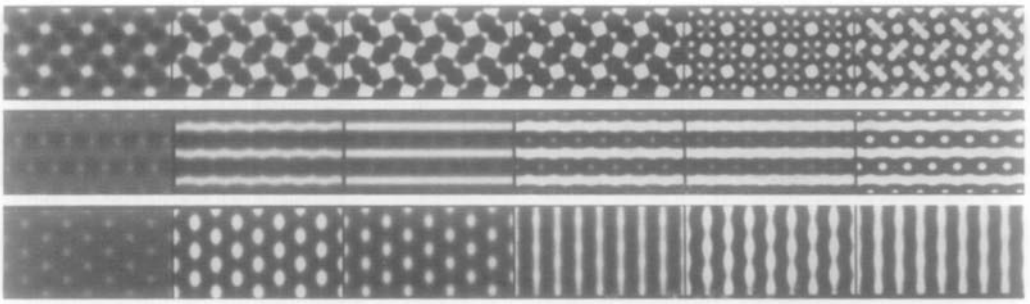

FIG. 11. Image simulations showing effect of increasing crystal thickness: at 500 kV, with C_s = 3.5 mm, and $\Delta f = -865$ Å . Top row, l. to r. [001], 31.9, 63.7, 95.6, 127.5, 159.3, and 191.2 Å; middle row, l. to r. [1$\bar{1}$1], 29.7, 59.4, 89.0, 118.7, 148.7, and 178.1 Å; bottom row, l. to r. [100] 28.4, 56.8, 85.3, 113.7, 142.1, and 170.5 Å.

cus for recording a "structure image" moves towards zero defocus with increasing thickness (*13*). As demonstrated later (Sect. 5), a completely unambiguous and accurate determination of focus and/or thickness may then not be possible without the simultaneous occurrence of some crystal defect. A single image from a small, unbounded, crystal region is certainly insufficient to determine uniquely the electron-optical parameters of the microscope.

Finally, a major problem with imaging small unit cell materials where relatively few diffracted beams contribute to the image is the periodic recurrence of Fourier or "self"-images with changes of focus (*14, 15*). This is typified by the [100] zone simulations where strong contributions from the 020 and 011 beams give quasi-periodic oscillations in image contrast with respect to defocus (The Fourier image periods, given by $2R^2/\lambda$, are 789 and 984 Å, respectively, where R is the lattice spacing and λ the electron wavelength.) Simulations for the focal range -2500 to $+500$ Å, and crystal thicknesses up to 200 Å, establish that the major oscillation of interest, namely that of black and white spots having the same configuration as the Sn ions in projection, has a period of about 790 Å. Note, however, that the actual defocus value at which a change-over in contrast occurs is thickness-dependent—for thicknesses up to about 60 Å there is an approximately linear shift in defocus of +100 Å for every 15-Å increase in crystal thickness.

Reasonable fits between simulated and experimental images from perfect crystals were obtained and Figs. 12a–c, for example, show small areas, in each of the three zones, taken from the experimental micrographs presented above: shown as insets on each are matching simulations. The numerical values of crystal thickness and objective lens defocus values should be regarded as reasonable values (rather than absolute) bearing the above provisos in mind.

5. Twin Boundary Structure

(*a*) *Models for (011) Twinning*

A number of models have been proposed for (011) twin intergrowths in structures based upon hexagonally close-packed oxygen arrays. For completeness, and since these could occur in SnO_2, the models are summarized here. Bursill and Withers (*16*), for example, described a reflection operation about an (011) plane of oxygen atoms in corundum, and showed how this produced an anion anti-phase (i.e., effectively a stacking fault in the anion lattice) thereby generating trigonal prismatic, tetrahedral,

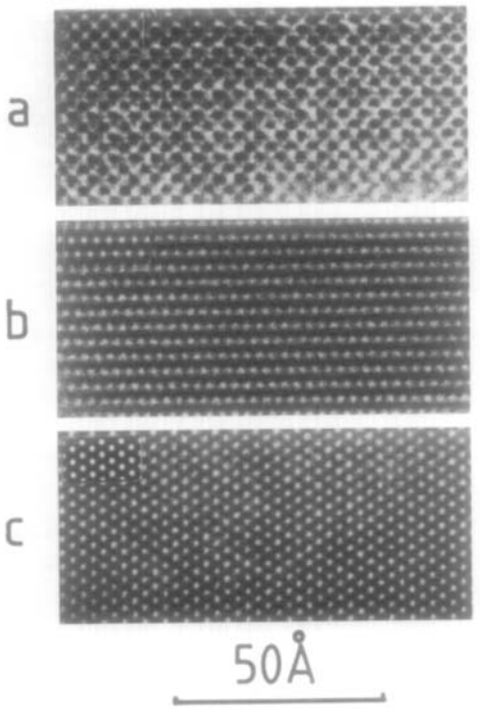

FIG. 12. Experimental 500-kV images with "matching" simulations inset (a) [001], $\Delta f = -1400$ Å, 31.9 Å thick; (b) [1$\bar{1}$1], $\Delta f = 0$ Å, 29.7 Å thick; (c) [100], $\Delta f = -900$ Å, 28.4 Å thick.

and square pyramidal sites at the boundary. Twinning is also well known as a crystal growth mechanism, as well as being proposed as a means of accommodating impurity atoms (e.g., (*17*). Thus, the observations by Pyke *et al.* (*1*) of twinning in Sb-doped SnO_2, but not in pure SnO_2, led to the reasonable suggestion that antimony cations could be located at the twin planes. These authors suggested a coherent Sb_2O_4 intergrowth within the SnO_2 matrix, which could be described as the replacement of anions at an (011) anion anti-phase with Sb^{3+} ions, allowing a slab of Sb_2O_4 to be accommodated by a displacement of the SnO_2 matrix. However, chemically induced twinning of the matrix is equally favorable (*17*) for accommodation of large foreign cations in rutile-type structures. Gatehouse and Nesbit (*18*) showed that an oxygen-rich MO_2 structure could be formed by twinning rutile slabs with reflection about (111) planes: in this case, removal of some oxygen atoms at the boundary provides pseudo-hexagonal tunnels wherein large cations could be located. Yoshida *et al.* (*19*) have recently described a glide twin in Ti_4O_7 having the symmetry operation $\frac{1}{2}\langle 1\bar{1}1\rangle$ (011) (referred to rutile-type indices). It appears as a direct reflection when projected in both the [1$\bar{1}$1] and [100] zones, and maintains essentially the same nearest-neighbor bonding at the boundary as in the parent matrix. It has since been shown (*20*) that no dislocations are necessary to explain the propagation or growth of this twin in Ti_4O_7 due to the presence of face-shared octahedra at *CS* planes. Bursill (1974) (*21*) discussed the $\frac{1}{2}\langle 1\bar{1}1\rangle$ (011) twin operation and its relationship to the α-PbO_2-type structure (or high-pressure polymorph of TiO_2). Mechanical (or deformation) twinning is common in brittle materials subject to high strain rates (*22*) and often occurs in TiO_2 crystals which are thinned for electron microscopy by fracture techniques.

(*b*) *Image Matching Glide Twin*

Some of the models described above for the (011) twin intergrowth can be excluded as being unlikely for the SnO_2 twin, simply by comparison of the misalignment of atomic rows across the twinned lamellae with the misalignment of details in the experimental series (Fig. 8). Twins generated by reflection about an anion plane (Figs. 13a and b) introduce a (011) lamellae that is not an integral number of (011) planes in width and would therefore require considerable structural strain to give the experimentally observed misalignment in detail. Furthermore, the appearance and geometry of image contrast (e.g., Fig. 8d) is consistent with a reflection, in projection at least, about a cation plane (Fig. 13c). Pure reflection about an (011) cation plane results in unrealistically close anion–anion separa-

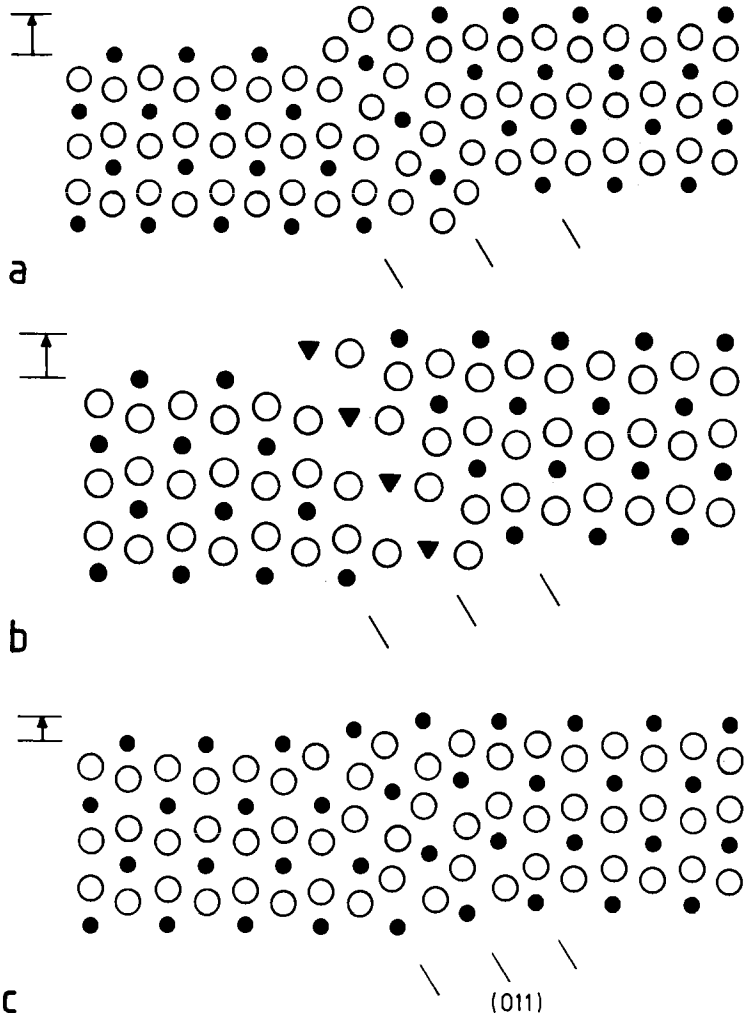

FIG. 13. Structural models for the (011) intergrowth projected along [100]. Large open circles represent oxygen atoms and small filled circles represent octahedrally coordinated cations. (a) Multiple twin formed by reflections about two (011) oxygen planes; (b) single reflection about a (011) oxygen plane with oxygen atoms substituted by cations (filled triangles); (c) multiple twins formed by a $\frac{1}{2}\langle 1\bar{1}1\rangle$ (011) glide operation on two (011) cation planes. Note the different separation of (011) cation planes and the displacement (arrowed) of cation planes across the intergrowth for each model.

tions whereas this is not the case for the twin generated by the operation $\frac{1}{2}\langle 1\bar{1}1\rangle$ (011).

The experimental series clearly starts at close to zero defocus (no visible Fresnel fringe) and, with increasing underfocus, has spot patterns near the crystal edge which can be termed White, Black, Black, White (strong), Black, and White for Figs. 8a–f, respectively. Black spots in Figs. 8b, c do not occur throughout the SnO_2 matrix, suggesting that both images are close to a black/white reversal as well as being thickness-sensitive. It is also known experimentally that the images are separated by *uniform* defocus steps having a value within the range 300 to 400 Å, and thus the focal series spans approximately 2 to $2\frac{1}{2}$ Fourier

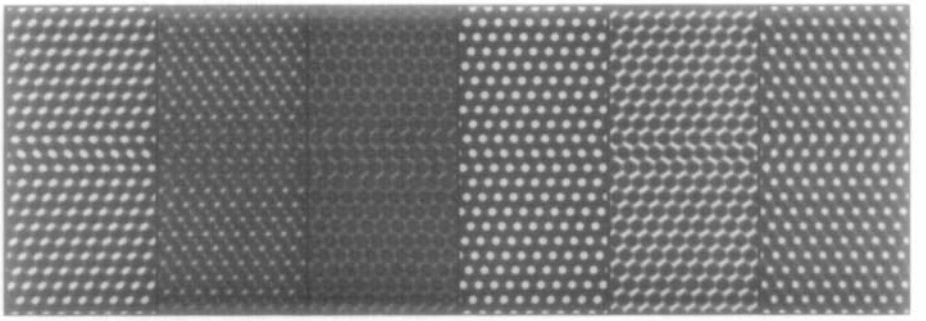

FIG. 14. Series of simulated images of (011) intergrowths generated by two $\frac{1}{2}\langle 1\bar{1}1\rangle$ (011) glide twins, giving closest fit with the experimental images of Fig. 8. Crystal thickness of 37.9 Å and defocus values of −26, −403, −780, −1157, −1534, and −1911 Å.

periods. Comparison of experimental images of the perfect SnO_2 matrix with computer simulations established good agreement for defocus steps between 320 and 380 Å and crystal thicknesses in the range 20 to 45 Å. Moreover, the location of the strong white spots seen in Fig. 8(d) are shown to correspond closely with the cation sites in projection.

Further consideration of Fig. 8 enables the thickness and defocus values to be more closely specified using the shift of black, or white, spots by $[0\frac{1}{2}0]$ away from the cation sites which occurs over approximately 500 Å change of defocus (e.g., on changing from $\Delta f = -400$ to -900 Å; see Fig. 10). Best agreement between the image simulations and the experimental images, including the defect region, was finally obtained for defocus steps between 375 and 380 Å. Assignment of more precise defocus values requires a better knowledge of crystal thickness, but any uncertainties remaining do not affect the model-sensitiveness of the image match. Finally, computer simulations of repeated (011) intergrowths, constructed by glide-twinning of the SnO_2 matrix by $\frac{1}{2}\langle 1\bar{1}1\rangle$ (011), show very good agreement with the entire through-focal series[1] even to the extent of showing the same *slight* misalignment along the cation rows seen in the experimental images (view obliquely along (010) and $(0\bar{1}1)$). This matching series, shown in Fig. 14, corresponds to defocus values of −26, −403, −780, −1157, −1534, and −1911 Å, respectively, and a crystal thickness of 37.9 Å. It is interesting and significant that this agreement is obtained without requiring any antimony at, or near, the boundary plane.

[1] A homogeneous projection of the structure has been assumed—this seems reasonable given the matching thickness of only ca. 38 Å.

(c) *Termination of (011) Intergrowth*

The Burgers vector associated with the termination of the (011) intergrowth seen in Fig. 8 can be conveniently measured on Fig. 8d. Thus, the missing vector in a Burgers loop is found to be somewhere between $[0, -\frac{3}{4}, 1\frac{3}{4}]$ and $[0\bar{1}2]$: this does not correspond at all well with the $\frac{1}{2}[1\bar{1}0]$ shear vector predicted for a Sb_2O_4 intergrowth.

The glide twin in Ti_4O_7 has been shown both to grow, and to propagate, without the need for dislocations (*19*)—these were considered to be energetically unfavorable. However, an essential feature of these twins, and of other twinning defects, was the inclusion of face-shared octahedra. Since SnO_2 does not normally form *CS* planes, it seems likely that dislocations are preferred rather than face-shared octahedra. Examination of the experimental image then suggests that the (011) intergrowth could be composed of two dislocations,

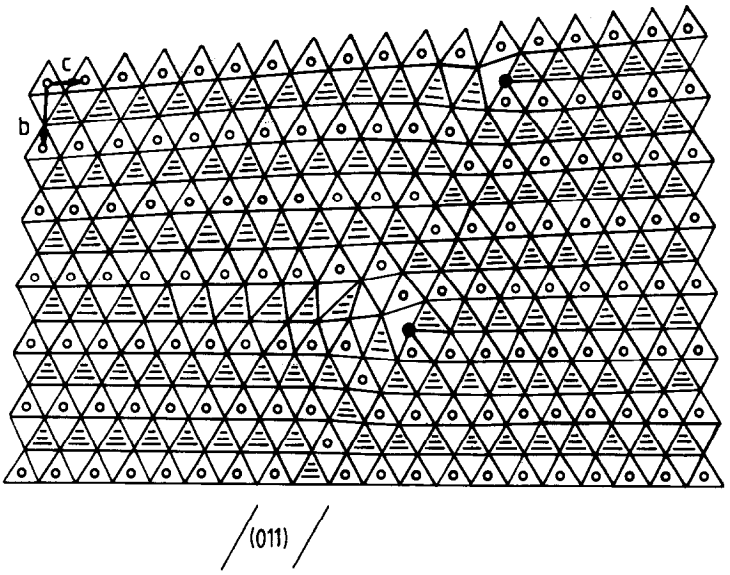

FIG. 15. Possible schematic model for the termination of the (011) intergrowth of Fig. 8, involving two dislocations. Shaded triangles represent faces of upward and downward facing octahedra. Filled circles indicate possible sites for Sb^{3+} ions at the dislocation cores.

namely $\frac{1}{2}[0\bar{1}1]$ and $\frac{1}{2}[0\bar{1}3]$, which add to give the required dislocation vector. This is drawn schematically in Fig. 15. Note that the second dislocation from the tip is longer as was observed experimentally. It seems plausible that these dislocations could be initiated by the presence of Sb as indicated. However, for several reasons, no attempt at image simulation and matching of the dislocations has been made. We have no independent method for estimating the extent of the strain field, or relaxation, in the vicinity of these dislocations, in particular lacking information about atomic positions. Moreover, a massive array size would be needed to simulate dynamic scattering for the entire defect, both because of periodic continuation effects and the need for fine enough sampling of reciprocal space. The demands on computer time and resources would simply be prohibitive.

6. Discussion and Conclusion

Whilst all possible structures for the observed (011) twin intergrowth have not been computed in detail, most could be discarded simply by comparison of the changes in geometry of the SnO_2 net projections on crossing the twin with experimental images, or eliminated by geometrical twinning operations which could not possibly be constructed with reasonable bond length and angles. Very close agreement was obtained between simulations of the glide twin, given by the operation $\frac{1}{2}\langle\bar{1}11\rangle$ (011), and an entire through-focal series. Nevertheless, the amount of computation needed even just to tie down the experimental parameters, such as focus and crystal thickness, in this relatively simple case of a glide twin suggests that structural studies of other types of extended defects, such as the dislocations shown in Fig. 15, will prove both difficult and time-consuming, particularly when atomic positions have to be derived from the supplementary information.

It is clear that the location of metal atom columns may be determined directly from experimental images in each of the three

projections, and thus the presence of any small defects should be indicated by HREM studies, given a reliable calibration of crystal thickness and objective lens defocus. Experimentally, these can only be obtained at present by recording a through-focal series, preferably using a wedge-shaped crystal, so that both focus and thickness variations are displayed. Observations at a single thickness and focus should generally be considered as unreliable for the purposes of model discrimination or for the detection of small defects. With regard to the latter, it is as well to recall the experimental series of Figs. 6 and 7 since the appearance of such amorphous material in some images could easily lead to erroneous conclusions concerning the nature of tin–antimony oxide catalysts (see (*2*)). The HREM images recorded in {001}, {100}, and {111} zone axes projections have not produced any unambiguous evidence for small defects which might reasonably be associated with the Sb-dopant: as reported by Pyke *et al.* (*1*), it was not possible to correlate twin content with Sb content. It is not even certain that the glide twin is associated with Sb at all, since mechanical deformation during specimen preparation may have resulted in mechanical twinning. It should also be appreciated that twinning may be initiated at small concentrations of Sb or Sb-rich precipitates (e.g., Sb_2O_4 particles), without necessarily having Sb incorporated systematically into the twin, as would have been the case for chemical twinning. Recent studies of small defects in TiO_{2-x} ($0 < x < 0.0035$) shows that twin lamellae may be terminated without dislocations if face sharing of octahedral sites is introduced (*23*).

Finally, we note the two experimental observations which have yet to be considered in detail, namely, the square array observed in [100] (labeled A in Fig. 5), and the apparent solitary *CS* plane (Fig. 3). Further experimental observations are in progress to establish whether these can be related to the presence of the Sb dopant.

Acknowledgments

Financial support for the Cambridge University 600-kV HREM project is received from the Science and Engineering Research Council (U.K.). L.A.B. is grateful to the Universities of Lyon and Melbourne for support of visits to Lyon and Cambridge during 1982.

References

1. D. Pyke, P. Reid, and R. J. D. Tilley. *J. Solid State Chem.* **25,** 231 (1978).
2. D. J. Smith, L. A. Bursill, and F. J. Berry, *J. Solid State Chem.* **44,** 326 (1982).
3. W. C. Nixon, H. Ahmed, C. J. D. Catto, J. R. A. Cleaver, K. C. A. Smith, A. E. Timbs, P. W. Turner, and P. M. Ross, "Developments in Electron Microscopy and Analysis 1977" (D. L. Misell, Ed.), pp. 13, Institute of Physics, Bristol/London (1977).
4. V. E. Cosslett, *Proc. R. Soc. London Ser. A* **370,** 1 (1980).
5. J. M. Cowley and A. F. Moodie, *Acta Crystallogr.* **10,** 609 (1959).
6. L. A. Bursill, A. R. Pring, D. J. Smith, and M. D. Shannon, *Philos. Mag. Part A* **45,** 771 (1982).
7. L. A. Bursill, A. R. Pring, D. J. Smith, and M. D. Shannon, in press.
8. H. Hashimoto, H. Endoh, Y. Takai, H. Tomioka, and Y. Yokota, *Chem. Scr.* **14,** 23 (1978/1979).
9. K. Izui, S. Furuno, T. Nishida, and H. Otsu, *Chem. Scr.* **14,** 99 (1978/1979).
10. R. W. G. Wyckoff, "Crystal Structures," Vol. 1, p. 251, Interscience, New York (1963).
11. A. R. Wilson, L. A. Bursill, and A. E. Spargo, *Optik* **52,** 313 (1978/1979).
12. A. R. Wilson, A. E. Spargo, and D. J. Smith, *Optik* **61,** 63 (1982).
13. M. A. O'Keefe and J. V. Sanders, *Acta Crystallogr. Sect. A* **31,** 301 (1975).
14. J. M. Cowley and A. R. Moodie, *Proc. Phys. Soc. London Sect. B* **70,** 486 (1957).
15. S. Iijima and M. A. O'Keefe, *J. Microsc.* **17,** 347 (1979).

16. L. A. BURSILL AND R. WITHERS, *Philos. Mag., Part A* **40,** 213 (1979).
17. S. ANDERSSON AND B. G. HYDE, *J. Solid State Chem.,* **9,** 92 (1974).
18. B. M. GATEHOUSE AND M. C. NISBET, *J. Solid State Chem.* **33,** 153 (1980).
19. K. YOSHIDA, Y. YAMADA, H. OTA, L. A. BURSILL, AND G. J. WOOD. *Philos. Mag., Part A* **44,** 73 (1981).
20. G. J. WOOD, L. A. BURSILL, Y. YOSHIDA, AND Y. YAMADA. *Philos. Mag. Part A* **46,** 75 (1982).
21. L. A. BURSILL, *J. Solid State Chem.,* **10,** 72 (1974).
22. P. BRAILLON AND J. SERUGHETTI, *Phys. Status Solidi A* **36,** 637 (1976).
23. L. A. BURSILL, M. G. BLANCHIN, A. MEBAREK, AND D. J. SMITH, *Radiat. Eff.* in press.